

Nonlinear dynamics in the flexible shaft rotating-lifting system of silicon crystal puller using Czochralski method

Hai-Peng Ren,^{1,*} Zi-Xuan Zhou,^{1,2} and Celso Grebogi^{1,3}

¹*Shaanxi Key Laboratory of Complex System Control and Intelligent Information Processing, Xi'an University of Technology, Xi'an, Shaanxi 710048, Peoples Republic of China*

²*North Minzu University Library, Yinchuan, Ningxia 750021, Peoples Republic of China*

³*Institute for Complex System and Mathematical Biology, University of Aberdeen AB24 3UE, United Kingdom*

(Dated: November 19, 2019)

Silicon crystal puller (SCP) is a key equipment in silicon wafer manufacture, which is, in turn, the base material for the most currently used integrated circuit (IC) chips. With the development of the techniques, the demand for longer mono-silicon crystal rod with larger diameter is continuously increasing in order to reduce the manufacture time and the price of the wafer. This demand calls for larger SCP with increasing height, however, it causes serious swing phenomenon of the crystal seed. The strong swing of the seed causes difficulty in the solidification and increases the risk of mono-silicon growth failure. The main aim of this paper is to analyze the nonlinear dynamics in the FSRL system of the SCP. A mathematical model for the swing motion of the FSRL system is derived. The influence of relevant parameters, such as system damping, excitation amplitude and rotation speed, on the stability and the responses of the system are analyzed. The stability of the equilibrium, bifurcation and chaotic motion are demonstrated, which are often observed in practical situations. Melnikov method is used to derive the possible parameter region that leads to chaotic motion. Three routes to chaos are identified in the FSRL system, including period doubling, symmetry-breaking bifurcation and interior crisis. The work in this paper explains the complex dynamics in the FSRL system of the SCP, which will be helpful for the SCP designers in order to avoid the swing phenomenon in the SCP.

I. INTRODUCTION

As the main material base for IC chip production, mono-silicon wafer production plays an important role in modern industrial field. The mono-silicon wafer is made from the mono-silicon rod produced by silicon crystal puller using the Czochralski (Cz) method [1]. In the Cz method, the polycrystalline silicon blocks are put into a crucible and melted by a heater surrounding the crucible at about 1420 °C. A mono-silicon seed hanged at the end of the flexible shaft rotating-lifting system is dropped into the melting silicon, provided the proper conditions are obeyed. As the flexible shaft rotating counterclockwise and the crucible rotating clockwise, the mono-silicon seed is slowly lifted upward to allow the new crystal growth. By precisely controlling the temperature gradients and the rate of lifting, a mono-silicon crystal ingot is extracted from the melt. During the whole procedure of the mono-silicon rod production, the FSRL system rotates and lifts the crystal rod at a certain rate determined by the technique parameters. The rotation of the mono-silicon crystal seed mixes the silicon melt and makes the crystal/melt surface to have a radius uniformity, which is essential for the quality of the mono-silicon crystal [2-4]. There is an increasing demand for longer mono-silicon crystal rods with increasing diameter in order to reduce the manufacture time and to improve the utilization rate of the wafer. Larger SCPs with increasing height being

put into usage lead to stronger swing phenomenon of the crystal seed. Specifically, in the seeding stage of crystal growth process, the swing phenomenon increases the risk of mono-silicon growth failure or causes defects in the growth of the silicon crystal. The engineering observation is that the swing amplitude and frequency suddenly become irregular under some circumstances. The SCP operator usually adjusts the rotation speed to avoid such unexpected irregular swing. But with the larger SCP size, this unexpected phenomenon becomes more frequent with even larger amplitude. How to characterize this phenomenon from a dynamical system viewpoint is of practical significance in the engineering field.

Up to now, few works have considered the dynamics of the swing phenomenon in the SCP. Yuan assumed the FSRL system to be like a double pendulum, and studied the relationship of the swing amplitude and the rotation speed (frequency) [5]. However, there are two weak points in that work: first, it is unreasonable to treat the FSRL system as a double pendulum, especially, at the initial stage of the mono-silicon rod growth from the melt; second, only simple oscillation is observed from the model without the systematical analysis of the whole dynamics. In a subsequent work [6], Yuan established a four-degree of freedom nonlinear dynamic equations by considering the in-plane and out-plane vibrations of the FSRL system. Then it deduced a linear approximation model of the system. Numerical simulations are given to show that the oscillation could be diminished by reducing the error of centration and by increasing the damping. However, it is also unreasonable to analyze the FSRL system by using

* renhaipeng@xaut.edu.cn

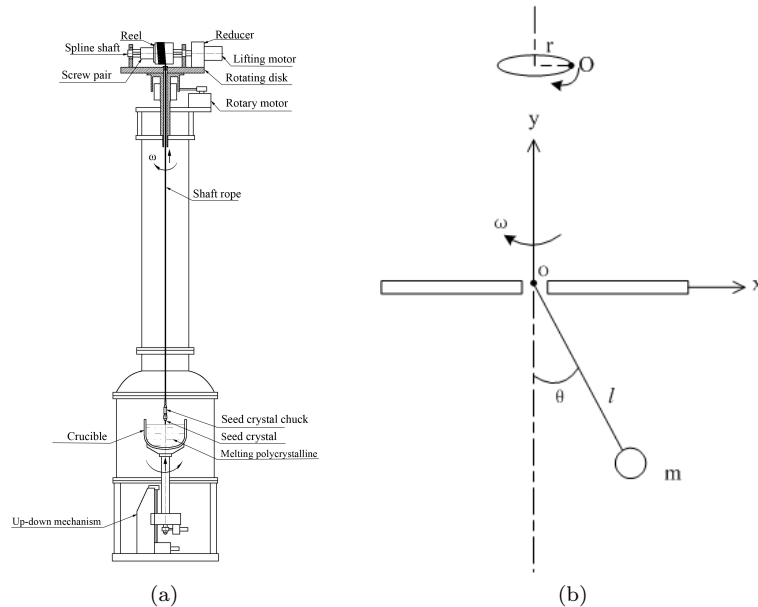


FIG. 1. (a) Structure diagram of flexible shaft rotating-lifting system of the Czochralski silicon crystal puller, and (b) its simplified model.

linear models, especially to address the oscillation. Moreover, the damping between the solid mono-silicon crystal seed and the liquid polycrystal melt is very small, and it cannot be increased or decreased. The irregular swing phenomenon and the underlying dynamics are still unclear, which need to be further and deeper investigated.

This paper is organized as follows. Section 2 describes the structure and working principle of the system. Section 3 introduces the mathematical modeling of the system. Section 4 uses Melnikov method to obtain the parameter region where chaos might exist. Section 5 studies the stability and bifurcation of the unperturbed system. Section 5 presents the numerical simulation to show the dynamic response of the system with perturbation, bifurcation diagrams, the Lyapunov exponents, phase trajectories, Poincaré sections, and power spectrum. Three routes to chaos are analyzed in section 6. Finally, section 7 summarizes the main results and the contributions of this article.

II. THE SYSTEM CONFIGURATION AND WORKING PRINCIPLE

The simplified structure diagram of SCP is given in Fig. 1a. From Fig. 1a, the puller consists of four parts, including the base pedestal usually placed underground to support the whole puller upside and the crucible up-down mechanism, the main body of the crucible and heater inside, the puller neck to hold the long crystal ingot rod, and the head with the rotating-lifting mechanism. The flexible shaft rope is curled around the reel mounted on the spline shaft driven by the lifting motor

through the reducer. The lifting motor regulates the lifting rate of the crystal ingot rod. A screw pair on the spline shaft is used to make the rotation shaft rope to be located at the center. All the lifting elements are installed on the rotating disk, which is driven by the rotating motor through the reducer. The rotation of the rotating disk drives the flexible shaft rotation around the center.

From the above description, we learn that the FSRL system can be treated as a pendulum with moving pivot, as shown in Fig. 1b. Works on parametrically excited pendulum has been reported in [7-12]. The models in those papers are usually abstracted from various actual mechanical devices, such as the mechanical components [13, 14], rotary cranes [15, 16], and energy converters [17]. Researches have shown that, a mathematical model like a rotating pendulum exhibit chaotic phenomena [18, 19]. The pendulum model in this paper, however, is different from the traditional parametric pendulum. Due to the imperfection of the manufacture, the rotating disk might have eccentricity, which makes the suspension point periodically varying. The way the suspension point O moves can be illustrated by the upper part in Fig. 1b. The period is decided by the rotating disk rotation frequency. In our model process, there is no linearization is considered, which reveal the nature of the nonlinear dynamics.

In order to explain the swing phenomenon and to understand the dynamics of the FSRL system, we establish the mathematical model of this system and analyze the dynamical characteristics of the FSRL system. The main purpose of this work is to demonstrate that the FSRL system can generate different kinds of motion, from periodic oscillations to chaos, when the rotational frequency

of the crystal is close to the natural frequency of the flexible shaft. We show that period doubling bifurcation, symmetry-breaking bifurcation and interior crisis can be present in the FSRL system. A better understanding of the FSRL system dynamics will help engineers to control the swing in an effective and efficient way in order to ensure a proper stable crystal growth environment.

III. MATHEMATICAL MODEL OF THE FSRL SYSTEM IN SCP

In this paper, we focus on the model of the FSRL system in the crystal seeding stage, in which the crystal seed (about 10 mm in diameter) can be treated as a mass point. Different from the previous double pendulum or 4 freedom oscillation equation, a pendulum with a moving suspension point is the feature of our model, where the moving of the suspension point is caused by the eccentricity of the rotating disk with respect to the center of the whole system.

The model is derived under the following three assumptions:

1. As the lifting speed is extremely slow with respect to the rotation, the length of the suspended flexible shaft can be treated as a constant.

2. The mass of the flexible shaft is neglected; the mass of the crystal chucks and (seed) crystal is assumed as a mass point.

3. Within the SCP, it is near vacuum state. The air damping of the system is too small to affect the system. The damping of the system is mainly caused by the interaction between the solid mono-silicon crystal rod(seed) and the polycrystalline silicon melt.

The simplified diagram of the FSRL system of SCP is shown in Fig. 1b. The rotation motors drives the rotating disk with angular velocity ω . The flexible shaft length is l , and the seed crystal together with ingot crystal has a mass m .

The system is considered to be a rotating pendulum, and the general nonlinear differential equations can be derived by using the second kind Lagrange's equation.

Define the angle between the rotational axis and the flexible shaft as the generalized coordinate, θ , as shown in Fig. 1b. The level of the rotating disk is assumed to be the zero potential energy surface. Then, the kinetic energy T and the potential energy V of the system are written as follows:

$$T = \frac{1}{2}m(l^2\dot{\theta}^2 + l^2\omega^2 \sin^2 \theta),$$

$$V = -mgl \cos \theta.$$

The Lagrangian of the system is, then,

$$L = T - V = \frac{1}{2}m(l^2\dot{\theta}^2 + l^2\omega^2 \sin^2 \theta) + mgl \cos \theta.$$

The periodic perturbed force caused by the eccentricity is given as:

$$Q_F = mr\omega^2 \cos(\omega t).$$

In the practical system, r is the eccentric distance. Using the Lagrange's equation, the dynamic equation of the rotating pendulum can be given as:

$$\ddot{\theta} = \frac{r}{l}\omega^2 \cos(\omega t) + \omega^2 \sin \theta \cos \theta - \frac{g}{l} \sin \theta - \frac{\xi}{m} \dot{\theta}, \quad (1)$$

where ξ is the damping coefficient. Introducing dimensionless time $\tau = \omega_0 t$, where $\omega_0 = \sqrt{g/l}$ is the natural frequency of the pendulum, and then the dimensionless coordinates $\theta \equiv \theta$, we have the dimensionless form of the dynamics as follows:

$$\ddot{\theta} = A\Omega^2 \cos(\Omega\tau) + \Omega^2 \sin \theta \cos \theta - \sin \theta - c\dot{\theta}, \quad (2)$$

where $\Omega = \frac{\omega}{\omega_0}$, $A = \frac{r}{l}$, and $c = \frac{\xi}{m\omega_0}$.

Equation. (2) can be rewritten as state space equations:

$$\begin{aligned} \dot{x}_1 &= x_2 \\ \dot{x}_2 &= A\Omega^2 \cos(\Omega\tau) + \Omega^2 \sin x_1 \cos x_1 - \sin x_1 - cx_2, \end{aligned} \quad (3)$$

where $x_1 = \theta$ and $x_2 = \dot{\theta}$. The dynamics of the flexible shaft rotating-lifting system is a two-dimensional non-autonomous system.

The phenomenon obtained by our model method is more reasonable to explain the practical observation, the on-going practice to control the swing also testifies the effectiveness of the model.

IV. ANALYSIS OF THE UNPERTURBED SYSTEM

The system without damping and perturbation is given by

$$\begin{aligned} \dot{x}_1 &= x_2 \\ \dot{x}_2 &= \Omega^2 \sin x_1 \cos x_1 - \sin x_1. \end{aligned} \quad (4)$$

System (4) is a Hamiltonian system and the Hamiltonian function is given by:

$$H(x_1, x_2) = \frac{1}{2}x_2^2 + \frac{1}{4}\Omega^2 \cos 2x_1 - \cos x_1. \quad (5)$$

By analyzing the fixed points of system (4) and their stabilities, we obtain the following results:

(i) For $\Omega < 1$, there is only one equilibrium $O(0,0)$, being the center.

(ii) For $\Omega > 1$, there are three equilibria including $O(0,0)$, being the saddle, $C_1(x_0, 0)$ and $C_2(-x_0, 0)$ being the centers, where x_0 is the positive root of x_1 satisfying $\Omega^2 \sin x_1 \cos x_1 - \sin x_1 = 0$.

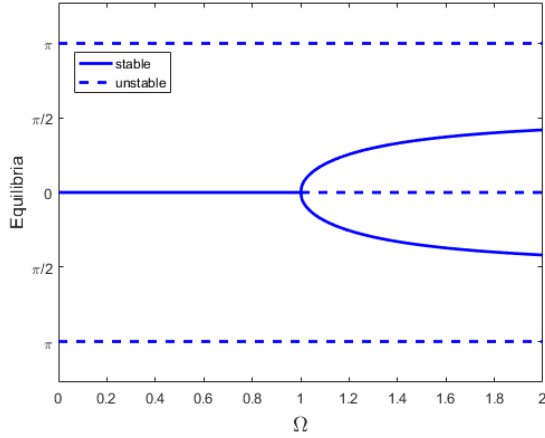


FIG. 2. Equilibria bifurcation diagram of system (4), where a pitchfork bifurcation is found, with stable equilibria given by *solid line* and unstable equilibria given by *dotted line*.

System (4) undergoes pitchfork bifurcation at $\Omega = 1$. The equilibria bifurcation diagram is given in Fig. 2. In addition, with the help of the Hamilton function (5), the trajectories can be classified by the different values of the Hamiltonian $H(x_1, x_2) = E$, which are marked in the corresponding phase portraits shown in Fig. 3. It can be seen that the phase structure of system (4) will change according to parameter Ω . In the case of $\Omega < 1$, the orbits for $E < E_0$ ($E_0 = 2 + \frac{1}{4}\Omega^2 \cos 2x_1 - \cos x_1$) are represented by a family of ellipses, it means the system moves periodically around the minimum of potential energy, as shown in Fig. 3a. When $\Omega > 1$, the phase portraits suddenly change into another structure, a pair of homoclinic orbits $q_+^0(t)$ and $q_-^0(t)$ connecting the origin to itself appear, plotted using red and blue solid lines, as shown in Fig. 3b, in the interior region of $q_+^0(t)$ and $q_-^0(t)$, there exists a family of periodic orbits.

Analytical expressions for the unperturbed homoclinic orbits can be derived by using Hamilton function (5). Notice that the solution of homoclinic orbits should satisfy the initial condition $(x_1(0), x_2(0) = (0, 0))$, and then $H(x_1, x_2)|_{(0,0)} = \frac{1}{4}\Omega^2 - 1$, we obtain:

$$x_2^2 = \frac{1}{2}\Omega^2 - 2 - \frac{1}{2}\Omega^2 \cos 2x_1 + 2 \cos x_1, \quad (6)$$

Equation (6) can be rewritten as follows:

$$\frac{dx_1}{dt} = \sqrt{\Omega^2 - 2 - \Omega^2 \cos^2 x_1 + 2 \cos x_1},$$

letting $\alpha^2 = \Omega^2 - 1$, it is rewritten as:

$$dt = \frac{dx_1}{\sqrt{\alpha^2 - 1 - \alpha^2 \cos^2 x_1 - \cos^2 x_1 + 2 \cos x_1}}.$$

Integrating both side of the above equation, we have:

$$t = \pm \frac{1}{\alpha} \cosh^{-1}(\alpha \cot \frac{x_1}{2}).$$

The above function can be transformed into:

$$x_1(t) = \pm 2 \cot^{-1}(\frac{1}{\alpha}) \cosh \alpha t.$$

From $x_2(t) = \frac{dx_1(t)}{dt}$, we obtain the $x_2(t)$ in the follow form:

$$x_2(t) = \mp \frac{2\alpha^2 \sinh \alpha t}{\alpha^2 + \cosh^2 \alpha t}.$$

We obtain the two homoclinic orbits:

$$q_+^0(t) = (2 \cot^{-1}(\frac{1}{\alpha}) \cosh \alpha t, -\frac{2\alpha^2 \sinh \alpha t}{\alpha^2 + \cosh^2 \alpha t}), \quad (7)$$

and

$$q_-^0(t) = (-2 \cot^{-1}(\frac{1}{\alpha}) \cosh \alpha t, \frac{2\alpha^2 \sinh \alpha t}{\alpha^2 + \cosh^2 \alpha t}). \quad (8)$$

The analytical expression of the homoclinic orbits of the unperturbed system obtained above enables us to investigate theoretically the chaotic motion in the original system.

V. PARAMETER REGION OF CHAOS EXISTENCE USING MELNIKOV METHOD

In this section, we will investigated the necessary condition for existing the chaotic motion in system (3) by using the Melnikov method. The Melnikov method is an analytical method to detect possible chaotic motion in Hamiltonian system. For a two-dimensional Hamiltonian system with the homoclinic or heteroclinic orbits, considering the perturbation of the system damping and periodic excitation, the distance between the stable and unstable manifolds of the system fixed point can be calculated by Melnikovs integration. If the distance is equal to zero, the stable and unstable manifolds cross each other transversally, and from that crossing, the system will become chaotic [20].

We introduce the following notation for system (3):

$$\dot{\mathbf{x}} = \mathbf{f}(\mathbf{x}) + \mathbf{g}(\mathbf{x}, t). \quad (9)$$

Here $\mathbf{f}(\mathbf{x})$ is the Hamiltonian system and $\mathbf{g}(\mathbf{x}, t)$ is the perturbation,

$$\mathbf{f}(\mathbf{x}) = \begin{pmatrix} x_2 \\ \sin x_1 (\Omega^2 \cos x_1 - 1) \end{pmatrix},$$

$$\mathbf{g}(\mathbf{x}) = \begin{pmatrix} 0 \\ A\Omega^2 \cos \Omega t - cx_2 \end{pmatrix}, \mathbf{x} = \begin{pmatrix} x_1 \\ x_2 \end{pmatrix}.$$

Considering a Melnikov function defined as follows:

$$M(\tau) = \int_{-\infty}^{+\infty} [f(q^0(t)) \wedge g(q^0(t), t + \tau)] dt \quad (10)$$

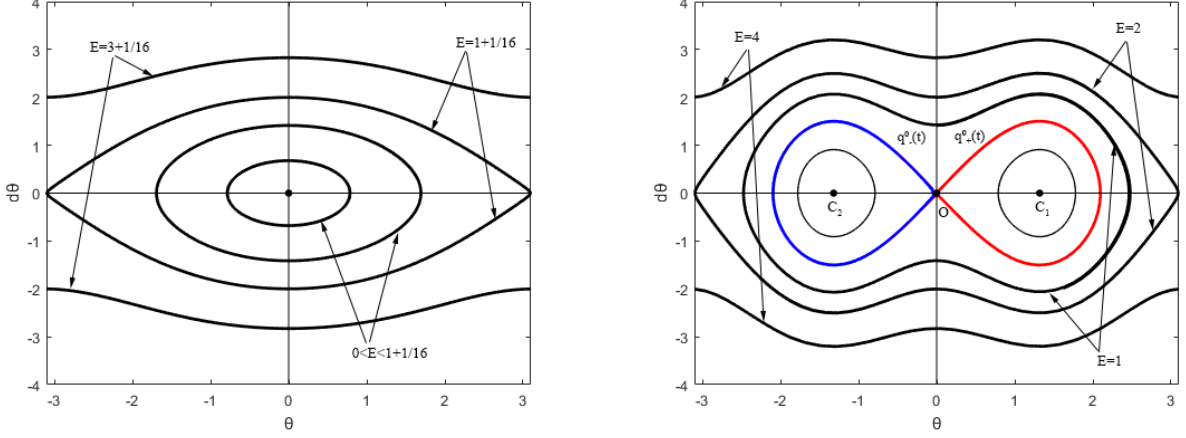


FIG. 3. (a) The phase portraits of system (2) for $\Omega = 0.5$, (b) the phase portraits of system (2) for $\Omega = 2$.

where operation " \wedge " is defined as:

$$(a_1, a_2)^T \wedge (b_1, b_2)^T = a_1 b_2 - a_2 b_1,$$

Then, the Melnikov function $M(\tau)$ for the homoclinic orbits $q_+^0(t)$ of system (3) is given by:

$$\begin{aligned} M(\tau) &= \int_{-\infty}^{+\infty} x_2(t) [A\Omega^2 \cos \Omega(t + \tau) - cx_2(t)] dt \\ &= \int_{-\infty}^{+\infty} -\frac{2\alpha^2 \sinh at}{\alpha^2 + \cosh^2 at} [A\Omega^2 \cos \Omega(t + \tau) \\ &\quad - c \frac{-2\alpha^2 \sinh at}{\alpha^2 + \cosh^2 at}] dt. \end{aligned} \quad (11)$$

The computation for $q_-^0(t)$ can be conducted similarly. Since $x_2(t)$ is an odd function, equation (11) can be rewritten as:

$$\begin{aligned} M(\tau) &= A\Omega^2 \int_{-\infty}^{+\infty} \frac{2\alpha^2 \sinh at}{\alpha^2 + \cosh^2 at} \sin \Omega t dt \sin \Omega \tau \\ &\quad - c \int_{-\infty}^{+\infty} \left(\frac{-2\alpha^2 \sinh at}{\alpha^2 + \cosh^2 at} \right)^2 dt. \end{aligned} \quad (12)$$

The integrals in equation (12) can be calculated by:

$$\begin{aligned} I_1 &= \int_{-\infty}^{+\infty} \frac{2\alpha^2 \sinh at}{\alpha^2 + \cosh^2 at} \sin \Omega t dt \\ &= 2\pi \sin \left[\frac{\Omega}{\alpha} \sinh^{-1}(\alpha) \right] \times \operatorname{sech} \left(\frac{\Omega \pi}{2\alpha} \right), \end{aligned}$$

$$\begin{aligned} I_2 &= \int_{-\infty}^{+\infty} \left(\frac{-2\alpha^2 \sinh at}{\alpha^2 + \cosh^2 at} \right)^2 dt \\ &= 4 \left[\frac{\ln(\sqrt{\alpha^2 + 1} - \alpha)}{\sqrt{\alpha^2 + 1}} + \alpha \right], \end{aligned}$$

By calculating the above integrals, Melnikov function is given by:

$$\begin{aligned} M(\tau) &= A\Omega^2 \times 2\pi \sin \left[\frac{\Omega}{\alpha} \sinh^{-1}(\alpha) \right] \times \operatorname{sech} \left(\frac{\Omega \pi}{2\alpha} \right) \times \sin \Omega \tau \\ &\quad - 4c \left[\frac{\ln(\sqrt{\alpha^2 + 1} - \alpha)}{\sqrt{\alpha^2 + 1}} + \alpha \right]. \end{aligned} \quad (13)$$

Melnikov's function (13) measures the distance between the stable and unstable manifolds in the Poincaré section. If for all τ the following inequality (14) holds, the system might demonstrate chaotic behavior in the sense of Smale horseshoes.

$$\frac{A}{c} \geq \left| \frac{2 \left[\frac{\ln(\sqrt{\alpha^2 + 1} - \alpha)}{\sqrt{\alpha^2 + 1} + \alpha} \right]}{\pi \Omega^2 \sin \left[\frac{\Omega}{\alpha} \sinh^{-1}(\alpha) \right] \times \operatorname{sech} \left(\frac{\Omega \pi}{2\alpha} \right)} \right| \quad (14)$$

The condition given in (14) is consistent with the following result shown in Fig. 5.

VI. DYNAMICAL BEHAVIORS OF THE FSRL SYSTEM

In order to investigate the dynamical behaviors of the full system (3), including the bifurcation diagrams, the Lyapunov exponents, and phase trajectories, Poincaré sections are used to show the complicated dynamics of system (3). Here, the fourth-order Runge-Kutta algorithm is used for the integration and the solution of the differential equations.

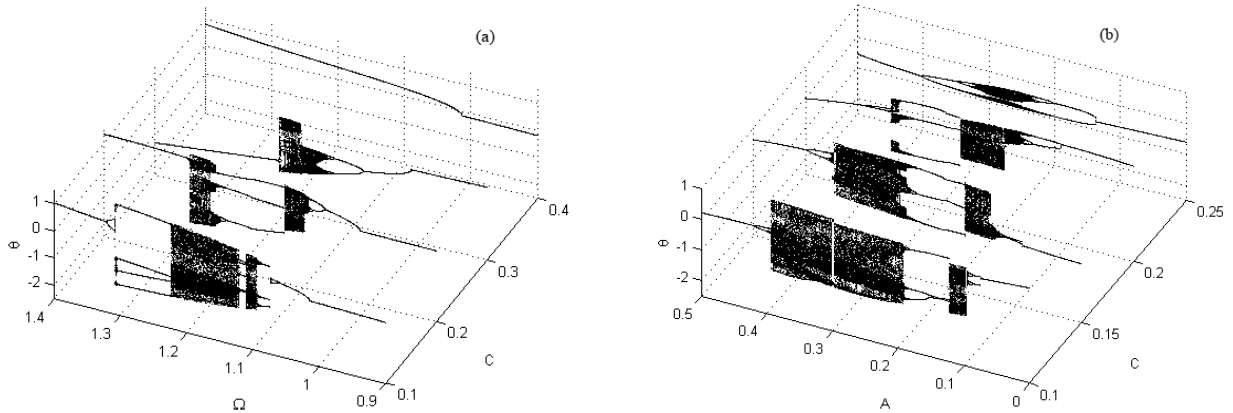


FIG. 4. The bifurcation diagrams of the system in three-dimensional space: (a) in (c, Ω, θ) space for $A = 0.2$, (b) in (c, A, θ) space for $\Omega = 1.1$.

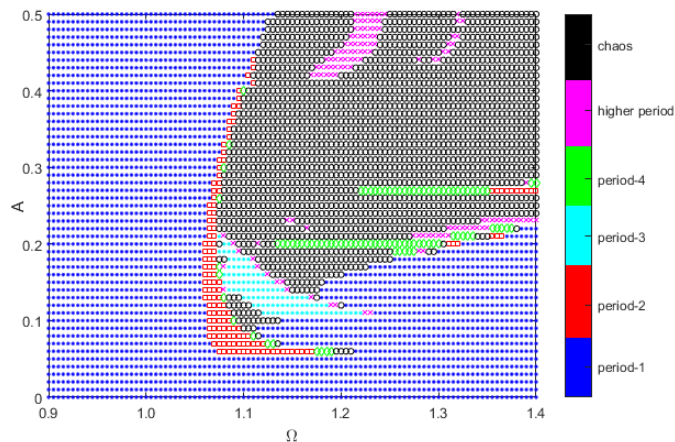


FIG. 5. Parameter space plot in the range of $\Omega \in (0.9, 1.4)$ and $A \in (0, 0.5)$, blue marks the period one motion, red marks the period two motion, green marks the period four motion, cyan marks the period three motion, magenta marks the higher period motion, and black marks the chaos.

A. Bifurcation diagrams

There are three parameters in system (3): the damping coefficient, the frequency and the amplitude of periodic excitation force caused by the eccentricity. The three-dimensional bifurcation diagrams of the system in space (c, A, θ) and (c, Ω, θ) are given in Figs. 4a and 4b, respectively. In Fig. 4a, A is fixed at 0.2, and in Fig. 4b, Ω is fixed at 1.1. It can be seen from Fig. 4a that: first, near the natural frequency, i.e., $\Omega = 1.1$, system (3) exhibits chaos, the smaller the damping is, the larger is the region of the parameter Ω having chaos; second, with the rotation frequency moving away from the natural frequency, the chaotic motion becomes a periodic oscillation; third, in the small damping coefficient range, there are periodic

motion windows; the smaller the damping coefficient is, the smaller is the periodic window width; fourth, in a practical situation, period one is desirable if the oscillation is unavoidable, which means that the rotation speed should be set away from the natural frequency of the system. In addition, the small rotation speed corresponds to small oscillation amplitude.

From Fig. 4b, for fixed $\Omega = 1.1$, we learn that: first, with the damping coefficient decreasing, the parameter range of the excitation amplitude, where chaos can be observed, becomes larger; second, there exists a periodic window between two chaotic parameter regions; third, with the damping coefficient decreasing, the chaotic parameter region becomes large. If the damping coefficient is large enough, chaos is eliminated.

Parameter space plot in Fig. 5 shows the different kinds of system responses when two parameters of the system are varied. It can be seen from Fig. 5 that: first, the system is in period one motion when the rotation frequency is less than the natural frequency; second, when the excitation amplitude is $A > 0.2$, it is easier for the system to be in a higher period or chaos; third, there are periodic windows in the chaotic region.

From the parameter space plot in Fig. 5, we know that, if the exciting amplitude is less than $A < 0.06$, the irregular swing can be avoided. This means that the irregular swing is disappeared if the eccentricity is small enough. And we also know that the irregular swing can be avoided by selecting the rotation speed less than $\Omega < 1.07$, which give the helpful guide for the operator of the SCP to set the process parameter.

The largest Lyapunov exponent (LLE) of a dynamical system is a quantity that characterizes the average exponential separation between two phase trajectories that are initially close by. In the chaotic region, the LLE must be positive. In the following, we give the LLE variation versus the parameter variation in order to clearly see the relationship of the LLE and the dynamics of the system,

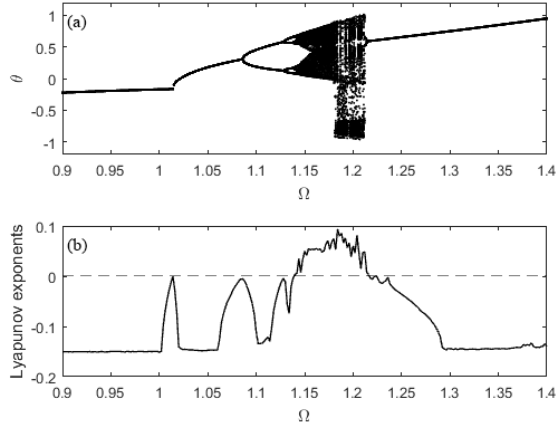


FIG. 6. (a) The bifurcation diagrams of the system for varying parameter Ω , and (b) the LLE corresponding to the parameter range in (a).

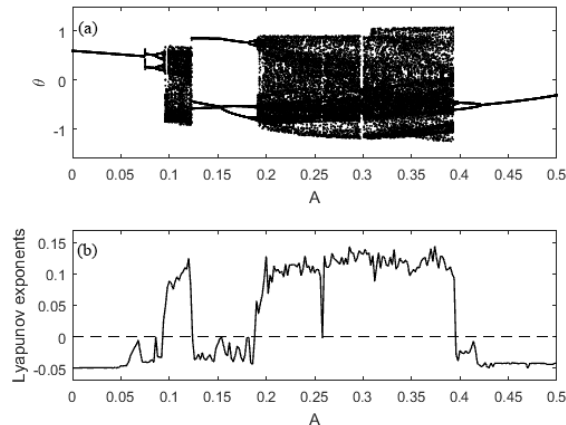


FIG. 7. (a) The bifurcation diagrams of the system for varying parameter A , and (b) the LLE corresponding to the parameter range in (a).

the bifurcation diagram with the same parameter variation is also given.

In the first case, A is fixed at 0.2 and the damping coefficient c is fixed at 0.3, then the LLE variation and the corresponding bifurcation diagram versus Ω variation are given in Figs. 6a and 6b, respectively. In the second case, Ω is fixed at 1.1 and the damping coefficient c is fixed at 0.1, then the LLE variation and the corresponding bifurcation diagram versus A variation are given in Figs. 7a and 7b, respectively. From Figs. 6 and 7, we know that in the chaotic parameter region the LLE is positive.

B. Routes to Chaos

a. A. Period doubling bifurcation

Period doubling bifurcation is one of the most common routes from periodic motion to chaos. From Figs. 4 to 7,

we can observe many examples of this route. To clearly see this point, we show the blow up bifurcation diagram within the range $\Omega \in (1.06, 1.16)$ in Fig. 6a, shown in Fig. 8a. From Fig. 8a, we know that when $\Omega \in (1.06, 1.087)$, period one is observed; when $\Omega \in (1.087, 1.129)$, period two is observed; when $\Omega \in (1.129, 1.137)$, period four is observed; afterwards, period eight and then chaos are observed. To see the different dynamical behaviors, we give the phase trajectories and the corresponding Poincaré sections for $\Omega = 1.068$, $\Omega = 1.115$, $\Omega = 1.133$, $\Omega = 1.139$, and $\Omega = 1.15$ in the upper panel and in the lower panel of Figs. 8b ~ 8f, respectively.

To see the time sequence of different periods and chaos, we give the time sequence for $\Omega = 1.068$, $\Omega = 1.115$, $\Omega = 1.133$, and $\Omega = 1.2$ and their corresponding power spectrum in the upper panel and lower panel of Figs. 9a ~ 9d, respectively. From Fig. 9, we surmise that the periodic oscillations are consistent with the corresponding power spectrum. In addition, chaos has a wide

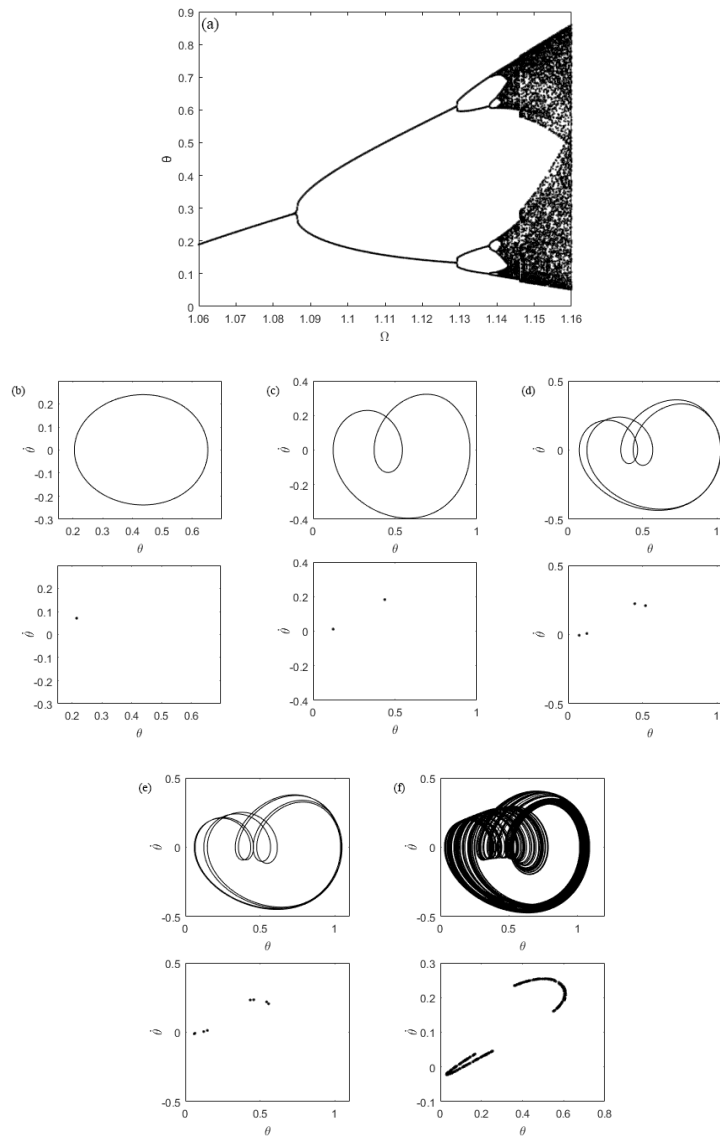


FIG. 8. (a) Local blow up bifurcation diagram shown in fig. 6(a) at $\Omega \in (1.06, 1.16)$. (b) The phase trajectory and Poincaré section point of period-1 oscillation at $\Omega = 1.068$ are shown in the upper panel and in the lower panel, respectively. (c) The phase trajectory and Poincaré section points of period-2 oscillation at $\Omega = 1.115$ are shown in the upper panel and in the lower panel, respectively. (d) The phase trajectory and Poincaré section points of period-4 oscillation at $\Omega = 1.133$ are shown in the upper panel and in the lower panel, respectively. (e) The phase trajectory and Poincaré section points of period-8 oscillation at $\Omega = 1.139$ are shown in the upper panel and in the lower panel, respectively. (f) The phase trajectory and Poincaré section points of chaos at $\Omega = 1.15$ are shown in the upper panel and in the lower panel, respectively.

spectrum.

b. B. Symmetry-breaking bifurcation

In Fig. 8a, a periodic window occurs when $A \in (0.125, 0.193)$. We notice that this periodic window are of period-3. In this interval, symmetry-breaking bifurcation takes place at $A = 0.1535$. To exhibit how the system enters chaos through symmetry-breaking route, a detailed bifurcation diagram is given in Fig. 10. In fact, Fig. 10 shows a blow up of a local region in the bifurcation diagram of Fig. 7a. The black points in Fig. 10 represent the symmetric period-3 oscillations, while the

blue and red points correspond to the two asymmetric period-3 solutions. For $A > 0.182$, the asymmetric solutions simultaneously undergo period doubling. Following the bifurcation cascades, finally chaos occurs. The system state is asymptotic to the blue asymmetric or the red asymmetric depending on the initial conditions [21].

c. C. Interior crisis

In this subsection, we show that there is another route to chaos, namely, interior crisis. In Fig. 6a, it can be observed that, at $\Omega \approx 1.18$, a small chaotic region suddenly enlarges into a larger one, which is a typical interior

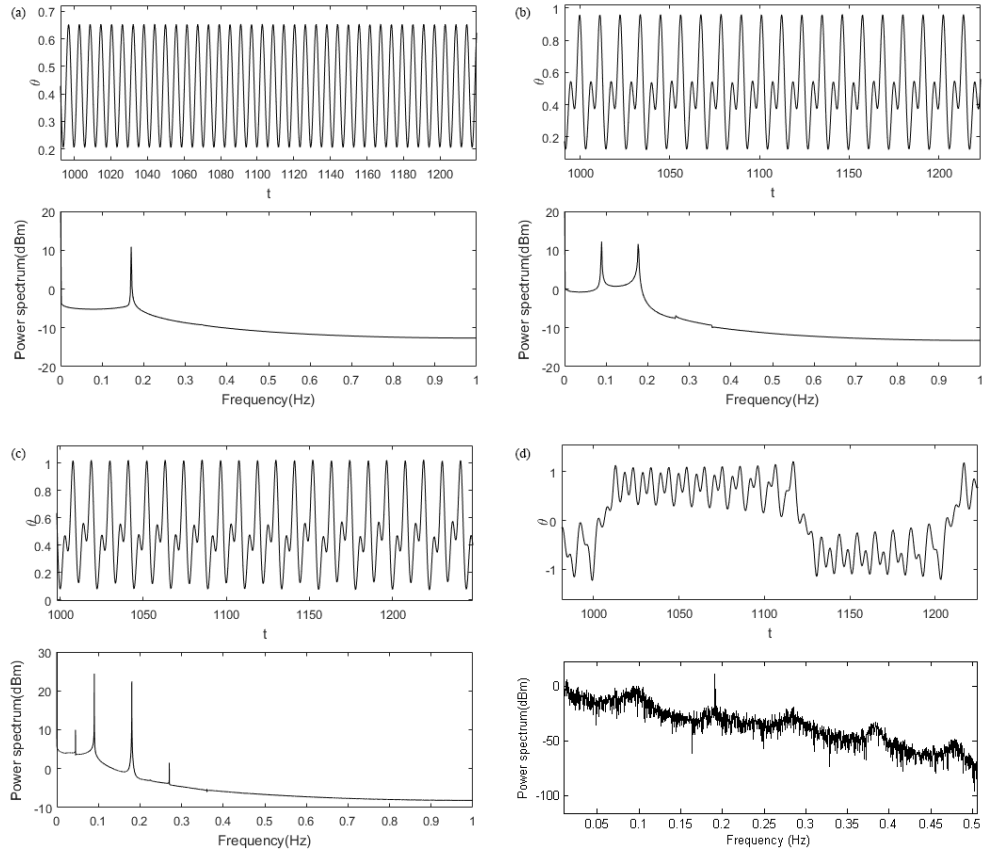


FIG. 9. (a) The time sequence and the corresponding power spectrum of period-1 oscillation at $\Omega = 1.068$ are shown in the upper panel and in the lower panel, respectively. (b) The time sequence and the corresponding power spectrum of period-2 oscillation at $\Omega = 1.115$ are shown in the upper panel and in the lower panel, respectively. (c) The time sequence and the corresponding power spectrum of period-4 oscillation at $\Omega = 1.133$ are shown in the upper panel and in the lower panel, respectively. (d) The time sequence and the corresponding power spectrum of chaos at $\Omega = 1.2$ are shown in the upper panel and in the lower panel, respectively.

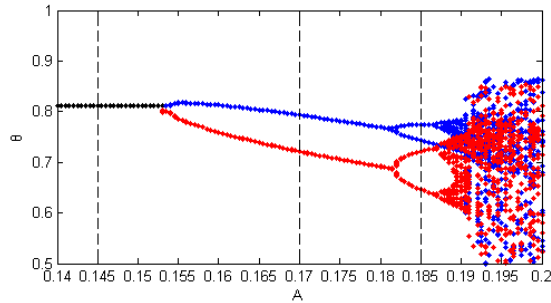


FIG. 10. An amplified window of Fig. 7(a) exhibiting symmetry-breaking bifurcation.

crisis phenomenon [22]. Figure 12 shows this change in the Poincaré section. This interior crisis, which is a type of global bifurcation, is another route to chaos when the parameter of the FSLR system varies.

The interior crisis can also be observed in Fig. 7a, where we can see that, for $A = 0.3$, there exist two isolated small chaotic region whose Poincaré section is

shown in Fig. 13a, while, for $A = 0.301$, there is one single large chaos region whose Poincaré section is shown in Fig. 13b. As parameter A passes the critical value, the size of the attractor is suddenly enlarged. The new blue Poincaré section points include the old red ones and new incremental blue points. This is a typical interior crisis phenomenon.

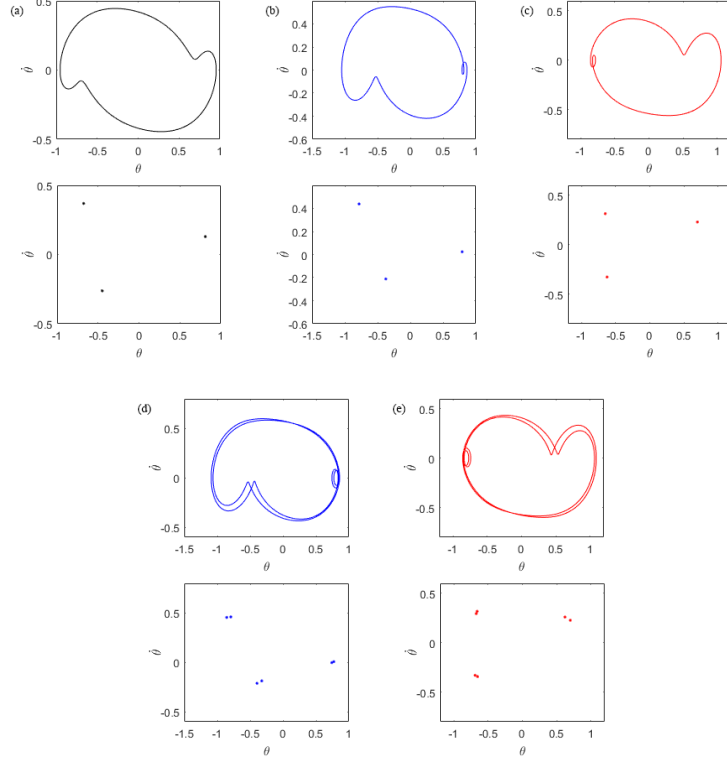


FIG. 11. The phase portraits and Poincaré sections for three different A values in the symmetry-breaking bifurcation in Fig. 10. Subplot (a) is the phase trajectory and Poincaré section for $A=0.145$. Subplots (b) and (c) are the phase trajectories and Poincaré sections for $A=0.17$ at different initial values; Subplots (d) and (e) are the phase trajectories and Poincaré sections for $A=0.185$ at different initial conditions.

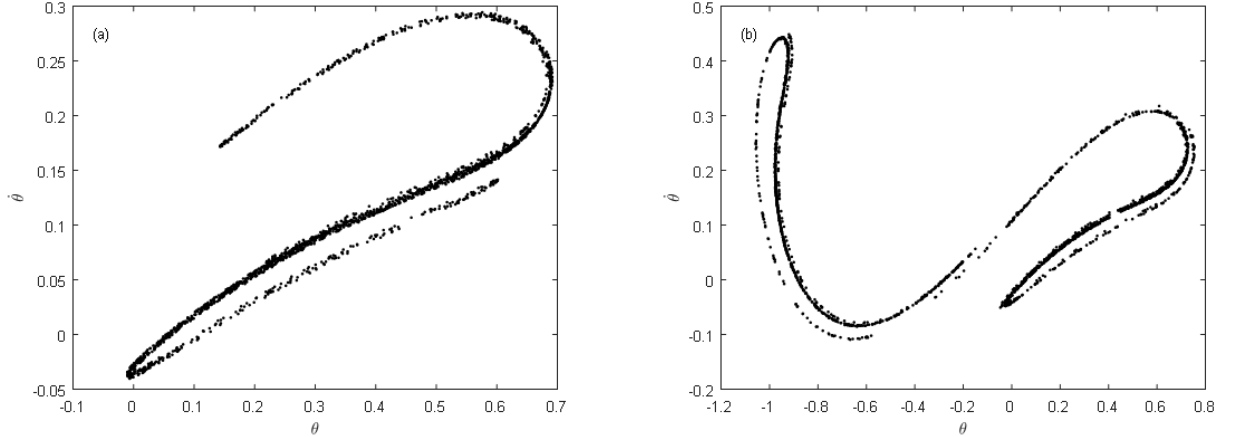


FIG. 12. (a) The Poincaré section of a small chaotic attractor at $\Omega = 1.17$ in the bifurcation diagram of Fig. 6(a). (b) The Poincaré section of a large chaotic attractor at $\Omega = 1.18$. in the bifurcation diagram of Fig. 6(a).

VII. CONCLUSIONS

In this paper, the dynamical model of the FSRL system of SCP is established based on the working principle of the FSRL system. The Melnikov method, the bifurcation diagram, the Lyapunov exponents, phase trajec-

tories, Poincaré sections and power spectra have been used to investigate the dynamical behaviors of the system. We learn from the analysis of this paper that: first, the rotation speed, i.e., the excitation frequency, the amplitude of excitation depending on the degree of eccentricity, and the damping coefficient affect the dynamical

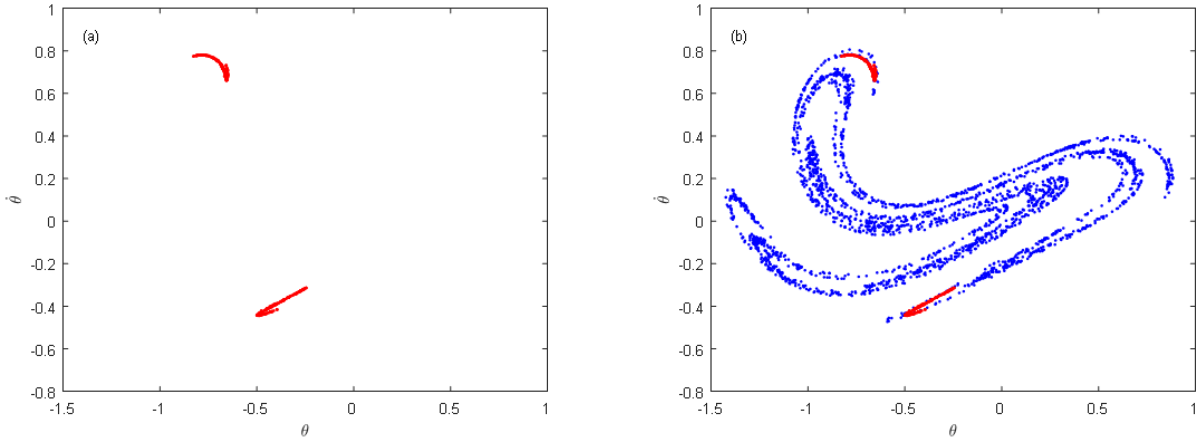


FIG. 13. (a) The Poincaré section of two isolated weak chaotic attractors located at $A = 0.3$ in Fig. 7(a). (b) The Poincaré section of a single strong chaotic attractor located at $A = 0.301$ in Fig. 7(a).

behaviors of the system; second, depending on different parameters, the system demonstrates a tremendous variety of different dynamical behaviors, including period-1, period-2, ..., and chaos; third, when the excitation frequency is close to the natural frequency of the system, complex behaviors, including high period and chaos occurs, which is consistent with the practical observations from industrial plants. We have shown three routes to chaos of the FSRL system, namely, the period doubling bifurcation, symmetry-breaking bifurcation, and the interior crisis route.

The complex dynamic characteristics of the system investigated in this paper explain the irregular swing phenomenon observed in the practical plants, and it provides a theoretical basis for eliminating the unexpected swing phenomenon of the FSRL system in the SCP using Cz method. Designing the eccentricity to be zero for the mechanical engineer is too challenge task to accomplish, therefore, designing an active controller to control the swing is a more feasible and adaptive method to deal with the swing problem, which will be given in the future paper.

-
- [1] Lan, C. W., 2004, "Recent progress of crystal growth modeling and growth control," *Chem. Eng. Sci.*, 59, pp. 1437-1457.
- [2] Kanda, I., Suzuki, T., and Kojima, K., 1996, "Influence of crucible and crystal rotation on oxygen-concentration distribution in large-diameter silicon single crystals," *J. Cryst. Growth.*, 166, pp. 669-674.
- [3] Liu, L, and Kakimoto, K., 2008, "Effects of crystal rotation rate on the melt-crystal interface of a CZ-Si crystal growth in a transverse magnetic field," *J. Cryst. Growth.*, 310, pp. 306-312.
- [4] Noghabi, O. A., M'Hamdi, M., and Jomâa, M., 2011, "Effect of crystal and crucible rotations on the interface shape of Czochralski grown silicon single crystals," *J. Cryst. Growth.* 318, pp. 173-177.
- [5] Yuan, D. N., Ma, J. P., Yang, R., Fu, W. P., and Liu, H. Z., 2008, "Dynamic simulation of oscillation phenomenon of single-crystal growth furnace lifting system based on double pendulum model," *J. Xi'an Univ. Technol.* 24, pp. 177-181.
- [6] Yuan, D. N., and Shi, J. W., 2010, "Vibration model and simulation for pulling system of single-crystal growth furnace," *J. Synth. Cryst.* 39, pp. 545-551.
- [7] Alasty, A., and Shabani, R., 2006, "Chaotic motions and fractal basin boundaries in spring-pendulum system," *Nonlinear Anal. Real World Appl.* 7(1), pp. 81-95.
- [8] Mann, B. P., and Koplow, M. A., 2006, "Symmetry breaking bifurcations of a parametrically excited pendulum," *Nonlinear Dyn.* 46, pp. 427-437.
- [9] Xu, X., and Wiercigroch, M., 2007, "Approximate analytical solutions for oscillatory and rotational motion of a parametric pendulum," *Nonlinear Dyn.* 47, pp. 311-320.
- [10] Belyakov, A. O., and Seyranian, A. P., 2014, "Homoclinic, subharmonic, and superharmonic bifurcations for a pendulum with periodically varying length," *Nonlinear Dyn.* 77, pp. 1617-1627.
- [11] Han, N., and Cao, Q., 2017, "A parametrically excited pendulum with irrational nonlinearity," *Int. J. Nonlin. Mech.* 88, pp. 122-134.
- [12] Depetri, G. I., Pereira, F., Marin, B., Baptista M. S., and Sartorelli J. C., 2018, "Dynamics of a parametrically excited simple pendulum," *Chaos.* 28, p. 033103.
- [13] Soto, I., and Campa, R., 2015, "Modelling and control of a spherical inverted pendulum on a five-bar mechanism," *Int. J. Adv. Robot Syst.* 12, pp. 1-16.
- [14] Reddy, B. S., and Ghosal, A., 2017, "Chaotic motion in a flexible rotating beam and synchronization," *J. Comput. Nonlinear Dynam.*, 12(4), p. 044505.
- [15] Yuan, G., Hunt, B., Grebogi, C., Ott, E., Yorke, J. A., and Kostelich, E., 1997, "Design and control of shipboard

- cranes,” *Proceedings of the ASME Design Engineering Technical Conference VIB. ASME 1997*.
- [16] Abdel-Rahman, E. M., and Nayfeh, A. H., 2002, “Pendulation reduction in boom cranes using cable length manipulation,” *Nonlinear Dyn.* 27, pp. 255-269.
- [17] Pan, J. N., Qin, W. Y., Deng, W. Z., and Zhou, H. L., 2019, “Harvesting base vibration energy by a piezoelectric inverted beam with pendulum,” *Chin. Phys. B*, 28(1), P. 017701.
- [18] Wiggins, S. S., 1988, “Chaotic dynamics of a whirling pendulum,” *Physica D* 31, pp. 190-211.
- [19] Chen, L. J., and Li, J. B., 2004, “Chaotic behavior and subharmonic bifurcations for a rotating pendulum equation,” *Int. J. Bifurcat. Chaos.* 14, pp. 3477-3488.
- [20] Melnikov, V. K., 1963, “On the stability of the center for time periodic perturbations,” *Math. Proc., Moscow Math. Soc.*, 12, pp. 3-52.
- [21] Bishop, S. R., Sofroniou, A., and Shi, P., 2005, “Symmetry-breaking in the response of the parametrically excited pendulum model,” *Chaos Soliton. Fract.* 25, pp. 257-264.
- [22] Grebogi, C., Ott, E., and Yorke, J. A., 1983, “Crises, sudden changes in chaotic attractors, and transient chaos,” *Physica D* 7, pp. 181-200.